FVTD Characterization of Substrate Effects for Archimedean Spiral Antennas in Planar and Conformal Configurations

Christophe Fumeaux, Dirk Baumann, Rüdiger Vahldieck
Swiss Federal Institute of Technology, ETHZ, IFH, 8092 Zürich, Switzerland
E-mail: fumeaux/dbaumann/vahldieck@ifh.ee.ethz.ch

Abstract — This paper describes the application of the Finite-Volume Time-Domain (FVTD) method to characterize the influence of the substrate on Archimedean spiral antennas. The unstructured mesh of the FVTD method permits to model precisely the fine spiral structure and the thin underlying substrate. Time-domain numerical results permit to demonstrate how the substrate affects the distribution of currents propagating on the metallic spiral arms. The substrate influence in the active region of the spiral is described through an effective permittivity which can be related to the transverse mode distribution on the arm of the spiral. Application of the FVTD method to conformal spiral geometries is also suggested in three examples.

Index Terms—FVTD, spiral antennas, conformal antennas

I. INTRODUCTION

Archimedean spiral antennas are characterized by their compactness and stable radiation performances over a large bandwidth. They have been therefore widely applied as circular-polarized broadband radiators. The Archimedean spiral is identified through its constant line width and fixed distance between successive spiral windings. Because of these fixed dimensions, it is not a truly frequency-independent radiator. However, circular polarization and remarkably stable radiation patterns are achievable over a bandwidth of more than one decade. The operational frequency limits of the spiral are determined by two radii that delimits the spiral extent: The lowest operational frequency of the spiral is determined by its outer radius which defines the overall dimensions of the device, and the upper frequency limit is set by the inner spiral radius, required to accommodate the physical extent of the feed in the spiral center. A typical Archimedean spiral antenna exhibits narrow arms and a large number of windings, making it a challenging problem for any computational method. Several authors have analyzed Archimedean spiral antenna problems using different numerical methods. The approaches include e.g., the method of moments (MoM) [1],[2], the finite-difference time-domain method (FDTD) [3]-[5] and the finite-element method boundary integral method [4],[6]. Depending on the method used, approximations are made such as a thin-wire formulation for the MoM or

the limitation to square spiral or spiral in free-space in FDTD.

In the present paper, a numerical analysis of Archimedean spiral antennas on a thin-substrate is performed using the Finite-Volume Time-Domain (FVTD) method. The main advantage of the FVTD technique is its geometrical flexibility which arises from its application in an unstructured mesh. For the presented analysis, the curved spiral geometry is approximated accurately using an inhomogeneous tetrahedral mesh. This permits to resolve the fine features of the overall structure, such as the spiral arms and the thin substrate, through adaptation of the cell size to the local geometrical requirements.

The numerical analysis presented in this paper is addressing two aspects of the modeling of spiral antennas. First, the influence of the thin substrate supporting the metallic spiral arms (Section III). Particularly the effect of varying the permittivity and thickness of the dielectric material is characterized through a detailed simulation of the current distribution on the spiral arms, the field distribution transverse to the arms and the polarization bandwidth. Second, the paper explores conformal geometries of spiral antennas on conical, spherical, and cylindrical surfaces comparing the radiation characteristics to those of the corresponding planar geometry (Section IV).

II. FVTD ANALYSIS OF THE SPIRAL ANTENNA

This section reviews the main steps that lead to the FVTD simulation of the Archimedean spiral. Details of the geometry of the spiral structure are given as well as on the discretization of the models and on the computational aspects.

A. The FVTD Method

The FVTD method has been introduced at the end of the 80's [7],[8] as a numerical technique to solve Maxwell's equation in an unstructured mesh. It is inspired from finite-volume techniques that solve conservation equations in computational fluid dynamics. In electromagnetic applications, the method uses a

conservative form of Maxwell's curl equations integrated over finite volumes V_i

$$-\frac{\partial}{\partial t}\iiint_{V_i} \vec{B}\,dv = \oiint_{\partial V_i} \vec{n}\times\vec{E}\,da$$

$$\frac{\partial}{\partial t}\iiint_{V_i} \vec{D}\,dv = \oiint_{\partial V_i} \vec{n}\times\vec{H}\,da \quad. \tag{1}$$

For discrete solutions of these coupled differential equations, the finite volumes V_i are defined as the elementary cells of a partition of the computational volume. The boundary of the volume V_i is the surface ∂V_i with outward-pointing normal vector $\vec{n}$. Among the several FVTD algorithm variations, the formulation applied in this investigation is characterized by a collocation of all field components (electric and magnetic) in space and time. Specifically, all field components are located in the barycenter of the tetrahedral cells and are updated simultaneously during the march-in-time iteration. The explicit update equations are obtained using a flux-splitting method [9] and second-order in time is obtained using a predictor-corrector scheme.

B. The Archimedean Spiral Antenna

An Archimedean spiral is defined in polar coordinates (ρ,ϕ) as

$$\rho = a_0(\phi + \phi_0) \tag{2}$$

where a_0 defines the winding tightness and ϕ_0 is the starting angle that determines the inner radius of the spiral. To define the metallization of the two arms of the spiral antenna, four such curves rotated in increment of 90 degree are needed. The 90 degree rotation angle results in a self-complementary spiral where the arm width d_S is equal to the inter-arm spacing.

The spiral modeled in this investigation is composed of 11 turns. It has an arm width $d_S = 0.25$ mm, an outer radius $R = 11.25$ mm, and an inner radius $r = 0.25$ mm. The metallic spiral is supported by a substrate with a thickness of $h = 0.254$ mm (Fig. 1). All these dimensions make the device a challenging problem for time-domain simulations because of the discrepancy between the different scales involved: The full length along each spiral arm is around $L_S = 400$ mm, which represents ~1600 times the arm width d_S.

C. Discretized Spiral Model

To create the discretized FVTD spiral model, the boundary surfaces are first triangulated, and a tetrahedral volume mesh is constructed on the basis of this surface mesh(Fig. 2).This unstructured mesh is advantageous for two main reasons. First, the triangular discretization ensures an accurate approximation of the spiral. Second,

an inhomogeneous tetrahedral mesh permits to adapt locally the cell size to the dimensions of the fine structures
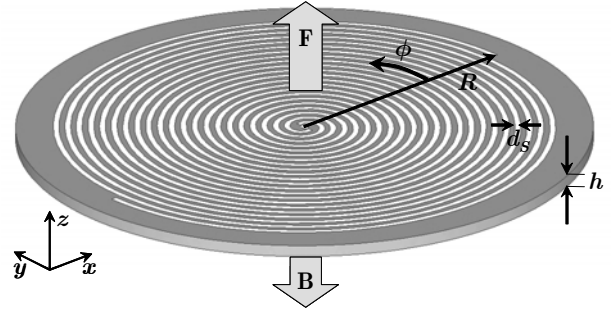

Fig. 1.   Geometry of the analyzed Archimedean spiral. The two-arm spiral consists of 11 turns and has a fixed arm width d_s of 0.25 mm. The thin substrate under the substrate is also represented. It breaks plane symmetry of the device and is used to define directions for front (F) and back (B) radiation.

that need to be resolved (here both, the fine spiral arms and the thin substrate). As illustrated in Fig. 2 for the discretized model, the linear size of the tetrahedrons grows quickly from $\sim \lambda_{min}/100$ in the close proximity of the spiral to $\sim \lambda_{min}/10$ in free-space, where λ_{min} is the smallest wavelength of interest. This inhomogeneity of the mesh keeps the total number of cells in the model at a reasonable level.

The transition from small cells to large cell can occur over a relatively short distance in a tetrahedral mesh. Nevertheless, a certain spatial range is required for the intermediate zone since a rapid transition decreases the mesh quality. The quality of a tetrahedron can be judged (among other criteria) by considering the ratio of its volume V_i to the sum of the area of its 4 faces S_k $(k=1,2,3,4)$. Tetrahedrons with elongated or flat shapes (i.e. that have a small volume/surface ratio) should be avoided as much as possible for best results. In addition, this ratio is used to determine the time step necessary for stable FVTD computation, according to [9]

$$\Delta t \leq \frac{1}{c}\min_i\left(\frac{V_i}{\sum_{k=1}^{4} S_k}\right) \quad. \tag{3}$$

Therefore, the "worst" or the smallest tetrahedron in the whole mesh determines the fundamental time step for stability. This requirement can be relaxed by combining the spatial inhomogeneity of the mesh to an inhomogeneous temporal discretization, implemented in the form of local time steps introduced in [10]. This scheme automatically separates the computational domain in sub-domains where time steps corresponding to power of two multiples $2^{\ell-1}\Delta t$ $(\ell = 1,2,3,...)$ of the fundamental time step Δt are applied. Typically, for the

type of inhomogeneity necessary to mesh the spiral, 5 levels of time steps are used, corresponding to local time steps between Δt and $16\Delta t$.
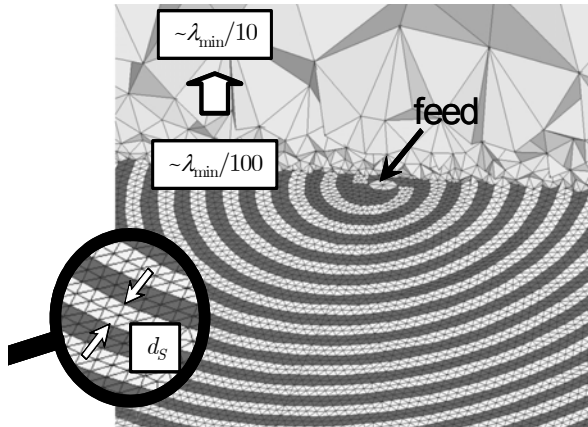

Fig. 2. Cut through the tetrahedral mesh of the spiral antenna. The lower part of the image shows the triangulation of the spiral plane, with a magnified view illustrating the resolution of the spiral arms.

D. Feed Model

In practical spiral antenna designs, a broadband balun is used for a balanced feeding of the radiating spiral. Simulations of such a practical balun has been demonstrated in [11] and compared to experimental data. The balun needs to be designed to provide nearly constant input impedance for the device over the operational frequency band. It is the component mainly responsible for the return loss of a practical spiral antenna.

The analysis of the balun can be in principle performed separately, and therefore, in the present simulation, a simple port is used to provide excitation of the spiral. The modeled port consists of 8 triangles located at the apex of the spiral (Fig. 2) where the excitation is provided through impressed electric fields between the starting points of the spiral arms. Both harmonic and broadband (1-20 GHz Gaussian pulse) excitations have been applied in this study.

E. Convergence and Computational Load

The side length of the triangles on the spiral plane corresponds to half the line width d_S (magnified view in Fig. 2). This fine discretization is necessary for the simulation to converge. It should be noted, that the strong inhomogeneity of the tetrahedral mesh permits to save computer memory. Despite a large number of triangles (>10k triangles per arm) on the spiral surface, a spiral model requires less than 250 MB computer memory (~400k tetrahedrons). Large simulation times however are necessary to allow the low-frequency components of the wave to propagate along the full length of the spiral arms, and to be reflected.

F. Validation

For validation of the analysis method, the FVTD simulation results of a practical cavity-backed spiral antenna have been compared to measurements. The device has been modeled including the 26 turns two-arm spiral, the thin-substrate, the absorber-loaded cavity, the balun and the fine feed (Fig. 3). Far-field data measured in an anechoic chamber showed an excellent agreement with simulation and provided validation of the numerical analysis. A full analysis will be published elsewhere.

III. RESULTS – SUBSTRATE EFFECTS

In this section, the effects of the substrate under the Archimedean spiral on the radiation properties are characterized through numerical analysis. The variation of substrate characteristics, such as permittivity and thickness, are related to changes in the simulated current distributions. A characterization of the observed effects is obtained by defining an effective permittivity in the active region of the spiral antenna.
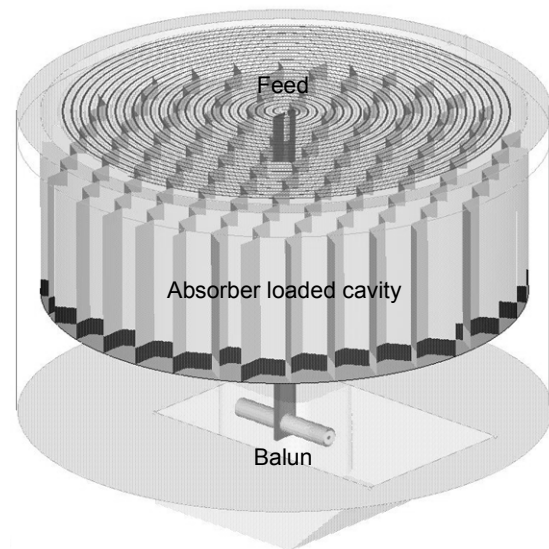

Fig. 3. Model of the cavity-backed Archimedean spiral analyzed for validation of the method. The substrate and the metallic housing of the device are shown transparent.

A. Substrate Permittivity Dependence

The current density on the metallic arms of the spiral is retrieved from the FVTD simulations. Instantaneous pictures of the current density at 8 GHz are shown in Fig. 4 for six different values of substrate permittivity. In these representations, the sign of the current density is defined considering the vectorial component of the current tangential to the spiral curve: A current propagating towards the outer end of the spiral is by convention positive, whereas a current directed toward the spiral feed is defined as negative.

The increase of the substrate permittivity ε_r is clearly apparent through the shrinking of the central area of the spiral where the current density distribution is visible. This shrinking is caused by the shortening of the effective wavelength λ_{eff} of the wave propagating along the spiral arms, which is defined introducing an effective permittivity ε_{eff} so that

$$\lambda_{eff} = \frac{\lambda_0}{\sqrt{\varepsilon_{eff}}} \ . \tag{4}$$

Classically, the active radiating region of the spiral is defined as annular band around a radius r_a where one full turn of the spiral corresponds to one effective wavelength, i.e.

$$\lambda_{eff} = 2\pi r_a \ . \tag{5}$$

Past the active region, the current density becomes insignificant, and the contribution to radiation irrelevant. The dashed circles in the six images of Fig. 4 indicate the circles with approximate radius of r_a. A more precise characterization is obtained by considering the current distribution along the arms, as demonstrated in the next paragraph.

B. Effective Permittivity

To estimate the effective permittivity in the active region, the current density is plotted as a function of the length of the path along the spiral arms, starting from the feed. Fig. 5 shows an example of this 1D representation of the instantaneous current distribution at 8 GHz. The active region corresponds to the location on the spiral where the effective wavelength λ_{eff} is equal to a turn length $\triangle L$ of the spiral (as highlighted in the figure at around 5-6 turns). There, the currents on adjacent arms of the spiral are nearly in phase. On the inner windings of the spiral, before the active region, the current distribution takes the form of a damped sinusoid. Past the active region, on the outer turns of the spiral, the current distribution exhibits a non-sinusoidal standing-wave characteristic shaped by reflections at the end of the arms and by crosstalk between the windings.

The effective permittivity ε_{eff} in the active region of the spiral is retrieved by measuring the effective wavelength λ_{eff} from graphs similar as the one represented in Fig. 5. The region taken into account for the estimation of ε_{eff} encompasses one turn of the spiral where $\lambda_{eff} \approx \triangle L$. The results of the analysis are represented in Fig. 6 for substrate permittivities ε_r ranging from 1.0 (free-space) to 12.0. The uncertainty grows with increasing ε_r, since the measured quantity λ_{eff} has a nonlinear dependence (4) on ε_{eff}.
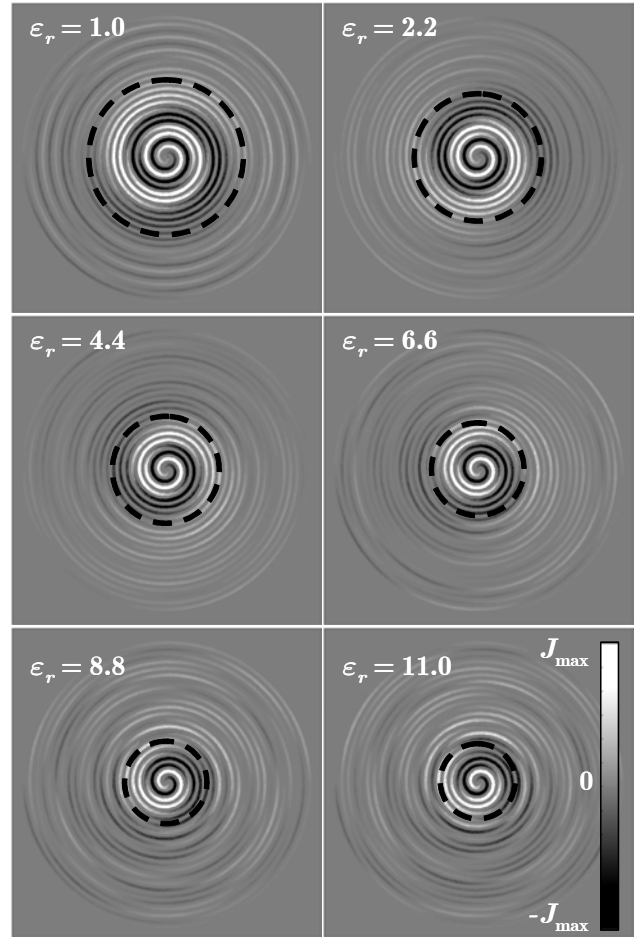

Fig. 4. Instantaneous current distribution on the spiral arms at 8 GHz for the six different permittivities ε_r indicated. The thickness of the substrate is equal to $h = 0.254$ mm. The dashed circles indicate the estimated location of the active region.
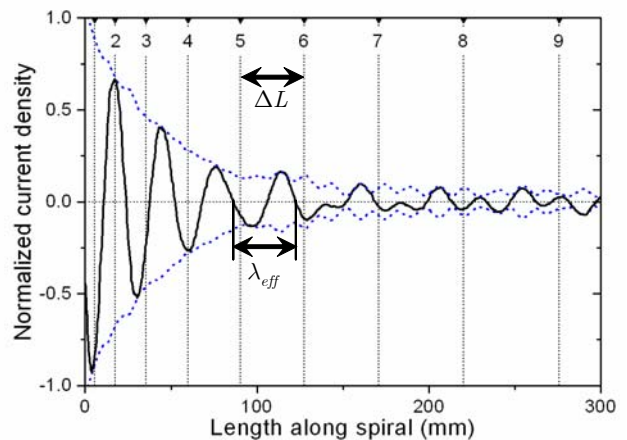

Fig. 5. Current distribution along the length of one spiral arm at 8 GHz. The permittivity of the substrate is $\varepsilon_r = 2.2$ and its thickness $h = 0.254$ mm. The instantaneous current distribution is shown as solid line and the envelope as dotted lines. The upper scale indicates the turns on the spiral.

For comparison, the effective permittivities of two different coplanar strip (CPS) line geometries (shown in Fig. 7) are also represented in Fig. 6 as a function of the substrate permittivity. The first of these geometries (CPS 1) corresponds to the transverse dimensions of two adjacent spiral arms, i.e. with both the gap width G and the strips widths W_1 equal to d_S. It is observed that the effective permittivity of the CPS computed from closed-form expressions [12] is higher than the ε_{eff} in the active region of the spiral. To obtain a good match between a CPS geometry and the spiral, wider strips are necessary. In the coplanar geometry CPS 2, the strips widths are doubled to get a resulting ε_{eff} dependence that matches that of the spiral.
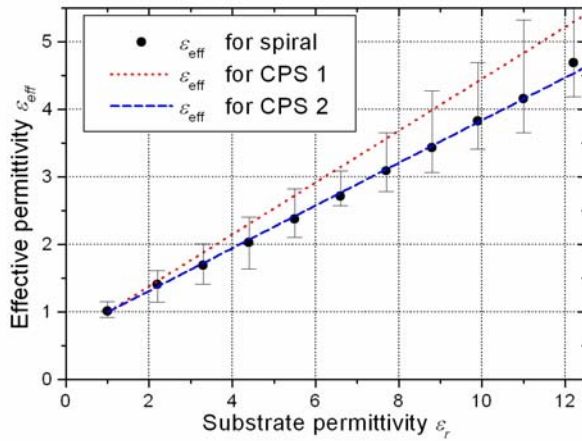

Fig. 6.   Estimated effective permittivity for the propagation of the waves in the active region of the spiral antenna as a function of the substrate permittivity. The error bars indicates uncertainty, which is mainly arising from the influence of the reflected waves. Also shown for comparison are the ε_{eff} of the coplanar strip (CPS) lines depicted in Fig. 7.
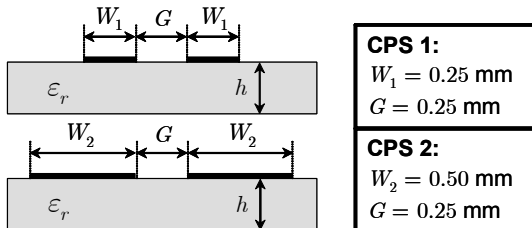

Fig. 7.   Transverse dimensions of the coplanar strips used for comparison of the effective permittivity with that in the active region of the spiral. The dimensions of CPS 1 correspond to the transverse dimensions of two adjacent spiral windings. CPS 2 considers an increased width of the conducting strips.

C. Substrate Thickness Dependence

In a second numerical experiment, the permittivity $\varepsilon_r = 4.4$ of the substrate is kept fixed, and the thickness h is varied. Fig. 8 shows the current distribution on the spiral for four different substrate thicknesses, from $h = 0$ (spiral in free-space) to $h \to \infty$ (semi-infinite substrate

in the lower half-space) for $\varepsilon_r = 4.4$. The variation clearly affects the effective permittivity that describes propagation of the currents on the spiral arms: As the substrate thickness grows, the active area shrinks towards the center of the spiral. However, by comparing the two bottom images of Fig. 8, it can be observed that increasing the substrate thickness past 1 mm does not change significantly the current distribution on the spiral arms.

The effective permittivity is then estimated on the basis of the simulations with the technique described in the previous paragraph (Sect. III B). The results for two substrate permittivities are shown in Fig. 9. In both plots, as the thickness of the substrate is increased, the effective permittivity rapidly increases from the value for a spiral in free-space ($\varepsilon_{eff} = 1$ for $h = 0$) to the asymptotic value

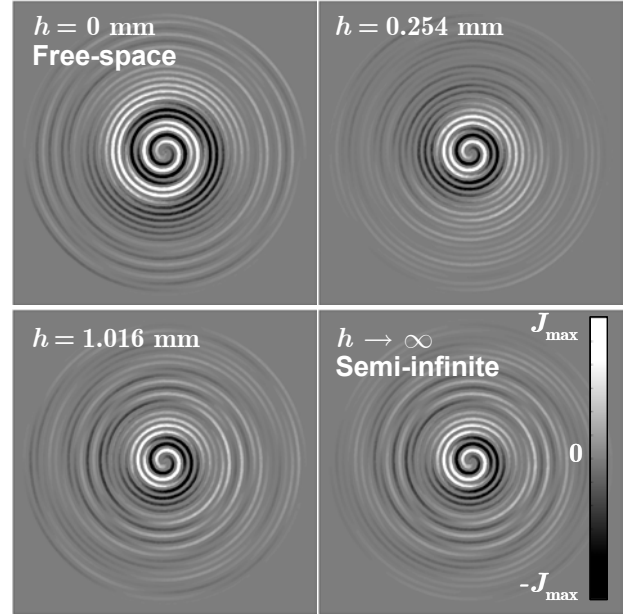$$\varepsilon_{eff}(h \to \infty) = \frac{\varepsilon_r + 1}{2} \ . \tag{6}$$

Fig. 8.   Instantaneous current distribution at 8 GHz for the spiral on a substrate with permittivity $\varepsilon_r = 4.4$ for four different substrate thicknesses h.

This asymptotic value is already nearly achieved, as anticipated from Fig. 8, for a substrate thickness of $h = 1$ mm. It should be mentioned that a nearly perfect match with the analytical value (6) is found for the ε_{eff}-values retrieved from the FVTD simulations. The same can be said about the value found for a spiral in free space. The consistency of these extremes provides an additional verification of the validity of the method used to estimate ε_{eff} from the results of the numerical analysis.

Also represented in the plots of Fig. 9 are the corresponding $\varepsilon_{eff}(h)$ curves for the two CPS lines of Fig. 7. As in Fig. 6, the best match to the numerical

analysis is not obtained from the CPS 1, which has strip widths corresponding to the arm width d_S of the spiral ($W_1 = d_S$), but from the CPS 2, with has broader strips ($W_2 = 2d_S$). An explanation for this phenomenon is given in the following paragraph.
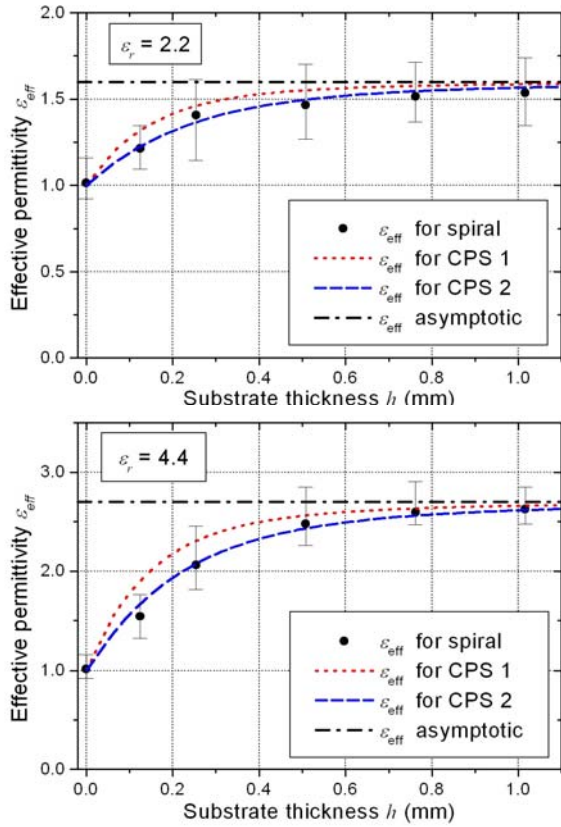

Fig. 9. Estimated effective permittivity of the propagation of the waves in the active region of the spiral antenna as a function of the substrate permittivity. Also shown for comparison are the ε_{eff} of the two coplanar strip lines depicted in Fig. 7 and the asymptotic value for semi-infinite substrate.

D. Transverse Field Distribution

The propagation properties of a wave on a transmission line are determined by the properties of the modes involved. For a CPS line, the fundamental mode is well-known: It is a quasi-TEM balanced mode, with the electric field in a transverse cross-section going from one strip to the other. Its propagation is best described through an effective permittivity ε_{eff}. Dependences of ε_{eff} on ε_r and h have been shown for two geometries with different strip widths (CPS 1 and CPS 2) in Fig. 7 and Fig. 9.

Despite a certain similarity between the transverse geometry of two adjacent spiral arms and that of a CPS, the propagation of currents along the spiral arms is different for the following reasons

- The spiral represents a system with a large number of adjacent coplanar strips.

- Although the feeding of the spiral is balanced, two adjacent arms of the spiral do not constitute a balanced system: the relative phase between adjacent arms depends on their location on the spiral.

Therefore, the transverse field distribution is expected to change significantly along the spiral arms, according to the phase difference between successive turns. To better visualize the sign (as defined in Sect. III A) of the instantaneous currents, the contrast of the grayscale current distribution representation in the spiral plane has been exaggerated in Fig. 10. Positive current density distribution is then represented as white and negative as black. The transverse field distributions are then considered in a plane perpendicular to the spiral plane, along a radial line, in the two ranges {1} and {2} indicated in Fig. 10.
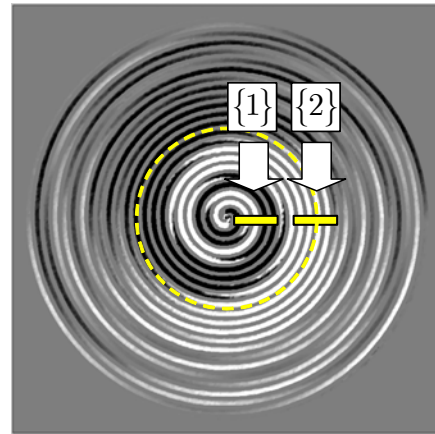

Fig. 10. Instantaneous current distribution on the spiral antenna at 8 GHz ($\varepsilon_r = 2.2$, $h = 0.254$ mm). The contrast is increased, so that the alternating black and white color basically indicates regions of opposite current directions on the spiral arms. The region {1} and {2} indicate the locations of the transversal cuts represented in Fig. 11, and Fig. 12, respectively. The dashed circle indicates the location of the active radius.

{1} The transverse field distribution in the inner turns of the spiral at a particular time is shown in Fig. 11. From this image, it is apparent that because the adjacent arms are at different potentials, the field lines are primarily confined in the direct vicinity of the strips. Starting from the left of the image, the E and H field distributions on the three first strips in Fig. 11 ($r = 0.5 - 1.75$ mm) resemble the field distribution of the dominant coplanar waveguide (CPW) mode. Continuing along the radial direction ($r = 2.0 - 2.75$ mm), the field lines between the last two represented strips resemble those of a CPS. Other instantaneous representations might show different patterns, but all share the characteristics that the fields are closely confined near the strips and that interaction is basically limited between adjacent arms.
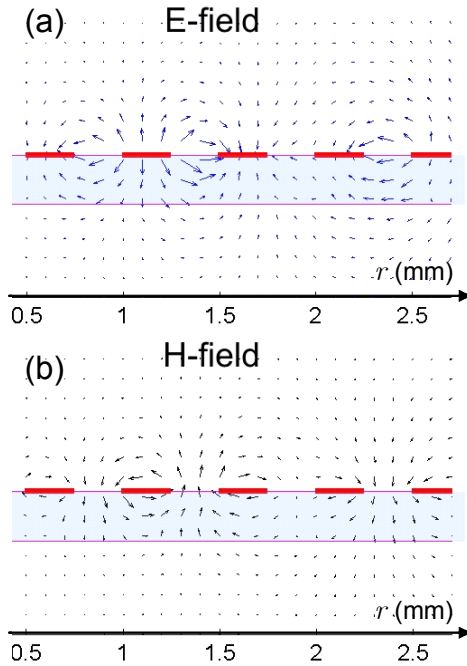
Fig. 11.   Vectorial representation of the transverse field distribution at 8 GHz in the center region {1} of the spiral antenna (r is the radius from the center of the spiral). The substrate is indicated by the shaded region and the spiral arms by line segments that represent cross-sections of the metallic strips. The arrows are normalized for good representation.
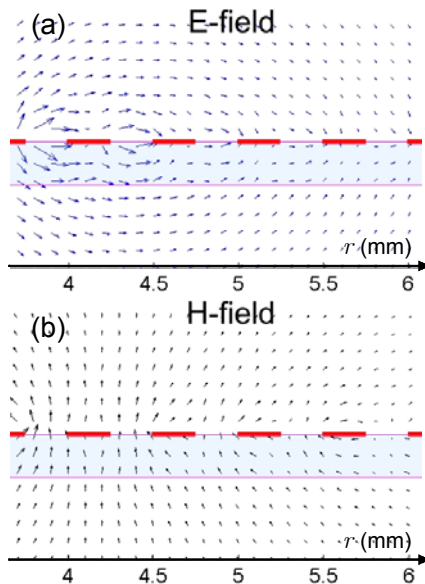

Fig. 12.   Vectorial representation of the transverse field distribution at 8 GHz in the active region {2} of the spiral antenna. The substrate is indicated by the shaded region and the spiral arms by line segments that represent cross-sections of the metallic strips. The arrows are normalized for good representation.

{2} Considering the transverse field distribution in the active region (Fig. 12), one observes a behavior different than in the inner turns. In the spiral active radiating region, adjacent arms are in phase, and therefore at nearly the same potential for all times. Therefore, the field lines show that interaction between strips extends farther than just to the adjacent arm, and the fields are much less closely confined than in the inner turns. This explains why the effective permittivity ε_{eff} in the active region of the spiral is lower than that of the CPS 1 that has corresponding transverse dimensions. Instead, ε_{eff} shows the same dependence as CPS 2, which has less confined fields because of its larger strips. The non-confined field distribution in the vicinity of the spiral arms in the active region is the cause for increased "radiation loss" of the considered coplanar structure.

The comparison of Fig. 11 and Fig. 12 illustrates why the propagation velocity on the spiral arms is not constant. In the more confined transverse field distribution of the inner turns, the effective permittivity is larger than in the outer turns, since most of the field lines under the spiral are located in the substrate. This effect is of course dependent on the frequency and this dispersive effect contributes to the chirp observed in broadband pulse excitation.

E.   Effect on the Radiation Characteristics

The analysis presented in this section is concerned with the near-field of the spiral antenna. However, the substrate configuration correspondingly influences the radiation characteristics. This paragraph shows how the lower frequency limit of the circular polarization bandwidth varies with the substrate permittivity of the spiral.

The low-frequency transition from linear polarization to circular polarization happens on a spiral antenna when the active radius approaches the outer radius of the spiral. Currents reflected at the outer end of the spiral are degrading the circular polarization purity. The low-frequency transition from linear to circular polarization is apparent through the following far-field characteristics (for increasing frequency):

- The axial ratio of the polarization ellipse decreases from a large value (indicating nearly linear polarization) and becomes smaller than the specified value for circular polarization (typically 3 dB).
- The phase between the orthogonal E-field components has a transition from 0 degree to 90 degree.

Fig. 13 and Fig. 14 show distinctly this low-frequency transition in axial ratio and phase, with a clear dependence on substrate permittivity. In Fig. 13 the approximated frequency of the 3 dB transition is displaced from higher than 5 GHz for the free-space spiral to about 2.6 GHz for $\varepsilon_r = 11.0$. This reduction factor of nearly 2 corresponds to $\sqrt{\varepsilon_{eff}}$, which confirms the data of Fig. 6.

Furthermore, the following general remarks can be made based on the numerical analysis of the spiral:

- For both the axial ratio and the phase, oscillations are observed in the transition region. These oscillations are caused by currents reflected from the spiral outer end. As the frequency increases, the reflected currents are reduced since the active region shrinks towards the spiral center.
- The polarization purity in the band of operation is slightly degraded by the presence of the denser substrate.

- The presence of the substrate causes an asymmetry that introduces a slightly higher radiation towards the back-side (substrate side). This effect becomes slightly more pronounced as the permittivity of the substrate increases resulting in a front-to-back asymmetry smaller than 0.5 dB.

- The input resistance in the operation range of the spiral is lower for substrates with higher permittivity ε_r. The results of the simulation give a value of ~120 Ω for the spiral in free-space. The value for $\varepsilon_r = 11.0$ is decreased to ~60 Ω. These values are obtained with a simple feed in the center of the spiral. A wideband balun is necessary in practice to provide balanced excitation over the operational bandwidth of the spiral and for matching purpose.

- The high-frequency limit of the spiral operation band is determined by the physical extension of the feed in the center of the spiral. The transition to linear polarization for broadside direction is -in this case- not the limiting factor and is therefore not apparent in Fig. 13 and Fig. 14. The higher operation frequency limit is determined by the degradation of the radial symmetry of the main beam.
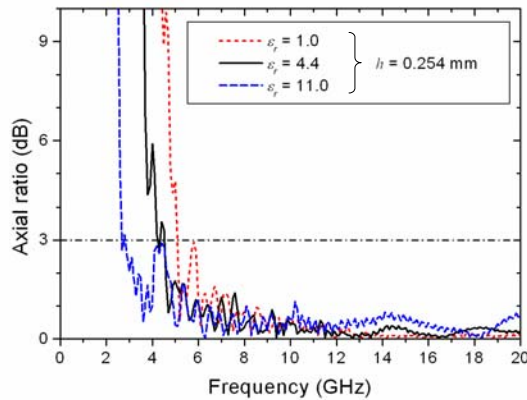

Fig. 13. Axial ratio of the polarization ellipse in broadside direction as a function of the frequency for three different substrate permittivities.
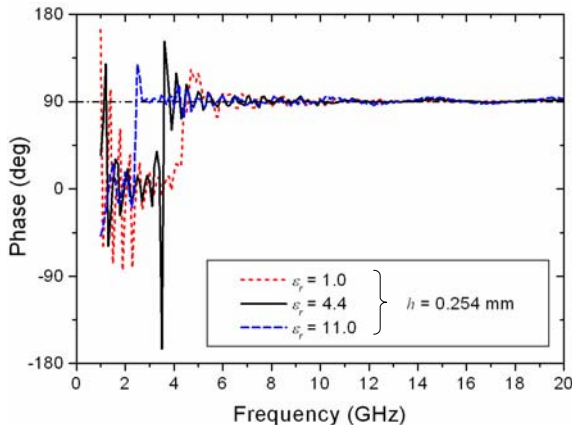

Fig. 14. Phase between the two orthogonal *E*-field components in broadside direction (far-field) as a function of the frequency for three different substrate permittivities.

IV. CONFORMAL SPIRAL ANTENNAS

In this section the radiation characteristics of spirals mounted conformally on non-planar substrates are investigated. Several examples are tested numerically: Spirals in (a) conical, (b) spherical and (c) cylindrical shape. The advantage of using the tetrahedral mesh is particularly evident in this case, since the FVTD simulation of such conformal structures imposes no additional computational cost over that of the corresponding planar geometry. In all conformal configurations presented below, the spirals have the same characteristic dimensions as in the planar configuration shown above, i.e. 11 spiral turns, arm width $d_S = 0.25$ mm, outer radius $R = 11.25$ mm, and inner radius $r = 0.25$ mm. All substrates have the standard thickness of $h = 0.254$ mm. The next section presents all studied configurations followed by a discussion of their radiation characteristics.
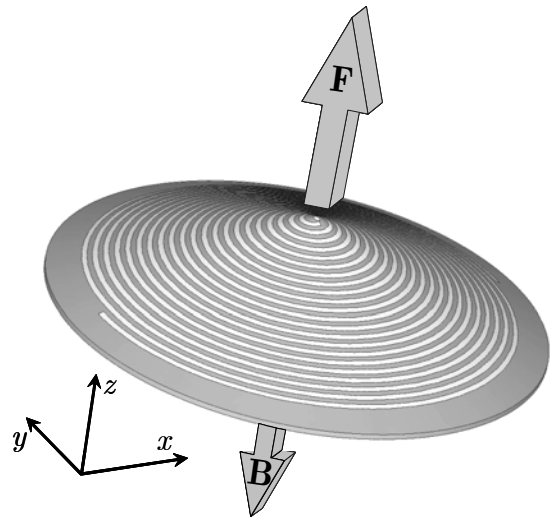

Fig. 15. Spiral antenna mounted on a conical substrate. The supporting cone has a height of 5 mm and a thickness of 0.254 mm. The spiral has the same geometry as the planar configuration (outer radius $R = 11.25$ mm). The front side of the antenna is defined in the direction showing towards the tip of the cone.

A. Conical Configuration

A conical arrangement (Fig. 15) with a base radius of 12.5 mm and a height of 5 mm is considered first. This conformal configuration is a well-known variation of spiral antenna design, the conical spiral antenna, characterized by an increased gain towards the front side. However in the present design, a very flat cone is considered, mainly with the aim of providing comparison with the spherical and cylindrical configurations.

B. Spherical Configuration

In the second conformal configuration, the spiral is mounted on a spherical surface. The curvature radius of the surface is 18 mm. This results in a total height (extent in z-direction) close to 5 mm for the configuration shown in Fig. 16.
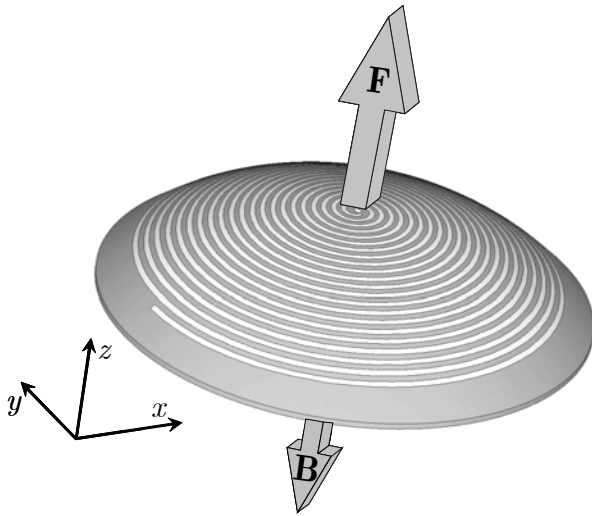
Fig. 16. Spiral antenna mounted on a spherical substrate. The substrate has a curvature radius of 18 mm and a thickness of 0.254 mm. The spiral has the same geometry as the planar configuration (outer radius R = 11.25 mm).

C. Cylindrical Configurations

Two different variations of the spiral mounted on a section of a cylinder have been analyzed. The two arrangements are distinguished by their different axis orientations with respect to the feed, as shown in Fig. 17. The curvature of the cylinder section exhibits the same radius as in the spherical case, i.e. 18 mm, and therefore has the same 5 mm total height for both cylindrical configurations.

D. Radiation Properties of the Conformal Geometries

The radiation performance of all three configurations is investigated in terms of:
    (i) Circular polarization purity (for broadside direction)
    (ii) Front-to-back ratio (F/B).
Both these characteristics are considered as a function of frequency.

(i) *Circular Polarization*
The circular polarization of the spiral is best described by the axial ratio of the polarization ellipse. Additional information is provided by the phase between the two orthogonal E-field components. For both the conical and the spherical configuration, the phase and the axial ratio are plotted in Fig. 18. From a comparison with the curves for the planar configuration (which is also shown in the figure), it can be concluded that for both cases, the integration on a non-planar substrate has no noticeable adverse effect on the polarization quality or on the low-frequency limit of the operational range. The reason for this result is the symmetry of the substrate geometries with respect to the spiral axis.

Axial symmetry is not present in both cylindrical geometries of Fig. 17 and thus an increased axial ratio (~1 dB) can be observed, indicating a degradation of the circular polarization purity (Fig. 19). In both orientations of the cylinder substrate, a spiral turn exhibits a saddle shape which affects the phase between the orthogonal field components in
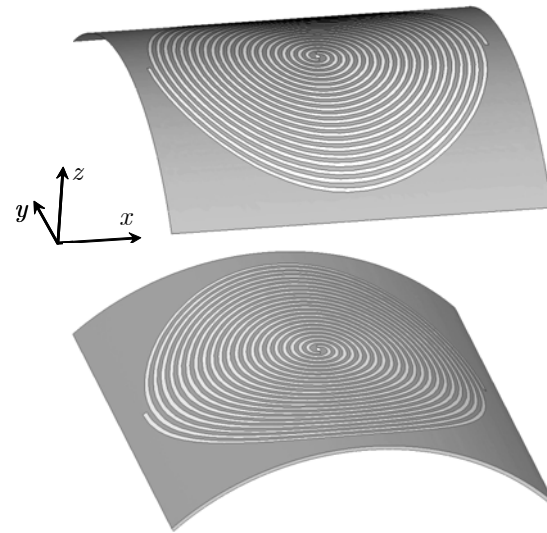

Fig. 17. Spiral antennas mounted on cylindrical substrates. The substrates have a curvature radius of 18 mm and a thickness of 0.254 mm. Top: Cylinder with axis in *x*-direction: bottom: Cylinder with axis in *y*-direction. The feed for both cases is oriented in *y*-direction. The spirals have the same geometry as the planar configuration (outer radius R = 11.25 mm).
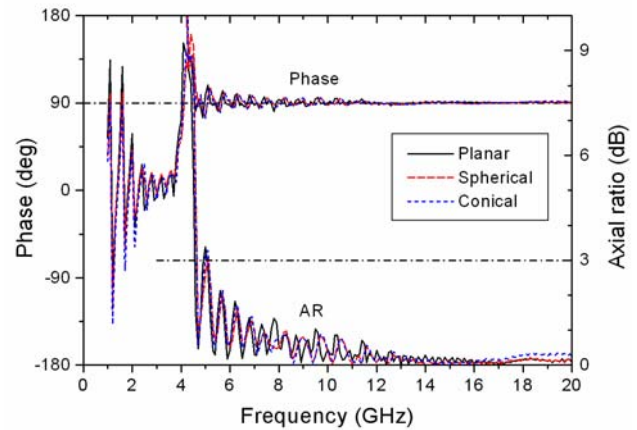

Fig. 18. Phase and axial ratio of the polarization ellipse in broadside direction (far-field on front side) as a function of the frequency for conical, spherical and planar configurations.
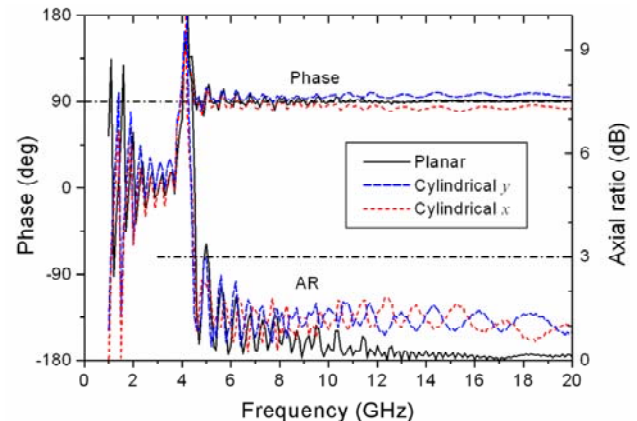

Fig. 19. Phase and axial ratio of the polarization ellipse in broadside direction (far-field on front side) for the two cylindrical configurations (Fig.17) as a function of the frequency, compared to the planar case.

the far-zone, altering the circular polarization. The deviation of the phase from the required 90 degree between the two orthogonal components is also visible in Fig. 19. The oscillations observed in the axial ratio are due to the frequency-dependent angular location of the active radiating region on the saddle shaped turns of the spiral. This is confirmed by the fact that the oscillatory behaviors of the axial ratios for the two orientations of the cylinder are 180 degree offset. Also, a variation of the effective permittivity (not shown here) affects the shape of the oscillations consistently, i.e. a smaller ε_r stretches the oscillations since the effective wavelength is larger.

(ii) *Front-to-Back Ratio*

The second radiation characteristic altered by the shape of the substrate is the F/B ratio (measured as ratio of radiated fields in +z vs. −z direction). The frequency dependence of this quantity is shown in Fig. 20 for the different geometrical configurations investigated. Depending on the shape of the substrate, different observations can be made:

- For the planar spiral, the presence of a substrate breaks the symmetry. For a thin substrate, this leads to a slight increase of the radiation towards the substrate side (F/B $\simeq$ -0.12 dB at 20 GHz).
- In the conical configuration, as expected, the pattern becomes more directive towards the front side. Due to the small height of the supporting dielectric cone, the F/B only reaches a maximum of 2.7 dB at about 9 GHz. For higher frequencies, the F/B ratio decreases because of the effect of the conical substrate, which now acts as a "reflector" (or "lens") towards the back side. This effect is demonstrated in Fig. 21 which shows the radiation patterns of the spiral at 9 GHz, i.e. near the frequency of maximum F/B ratio, and at 18 GHz, where the F/B ratio has decreased to 0.6 dB. The narrowing of the back lobe is clearly visible and becomes more pronounced as the frequency increases. Although the 3 dB beamwidth of the front lobe is in both cases close to 80°, the 3 dB beamwidth of the back lobe is reduced from 84° at 9 GHz down to 62° at 18 GHz.
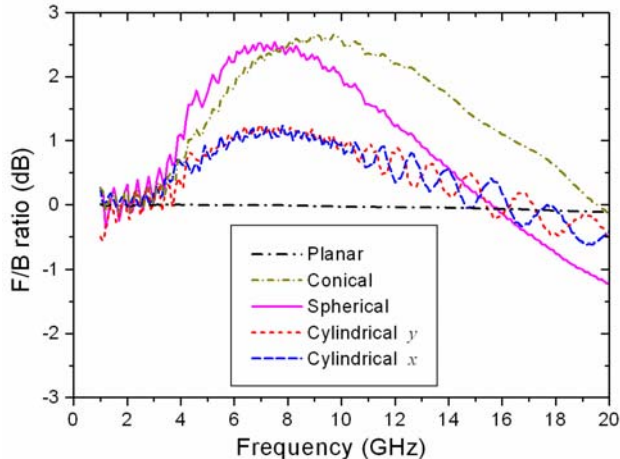

Fig. 20.   Front-to-back ratio as a function of the frequency for the four conformal spiral configurations compared to the planar case.

- For the spherical arrangement, similar observations as in the conical case can be made, with an overall increase of directivity for front radiation. This is expected because of the similarity with the conical configuration: Adjacent turns in the active spiral region correspond roughly to a conical arrangement with an angle α set by the tangential line to the sphere. In the spherical case, this flare angle α varies with the frequency-dependent location of the active region. For a particular frequency (and the associated active radius r_{a0}), the tangential line on the sphere has an angle corresponding to the flare angle α_0 of the conical arrangement (Fig. 22). In the present arrangement, this happens for a frequency of 6 GHz. Below this frequency, the angle α is sharper than in the conical case, which explains the displacement of the maximum F/B toward lower frequencies (maximum F/B occurs around 7 GHz) compared to the conical configuration. Again, the F/B ratio is shaped by two competing mechanisms with opposing effects: The increased directivity towards the front due to the non-planar shape, and the narrowing of the back lobe caused by the substrate acting as a reflector. For the spherical case, a negative F/B ratio past 16 GHz can be observed.
- For the two cylindrical configurations, the increase of the front-side directivity because of the convex shape is less pronounced than in the spherical case. In addition, oscillations (with 180 degree offset between both orientations) are also visible at the higher frequencies because of the saddle shape of the spiral turns. In the cylindrical configuration, the substrate exhibits only one radius of curvature in a particular direction and therefore, both effects observed (increase of front-side radiation and narrowing of the beam towards the back) are restricted to one angular dimension.
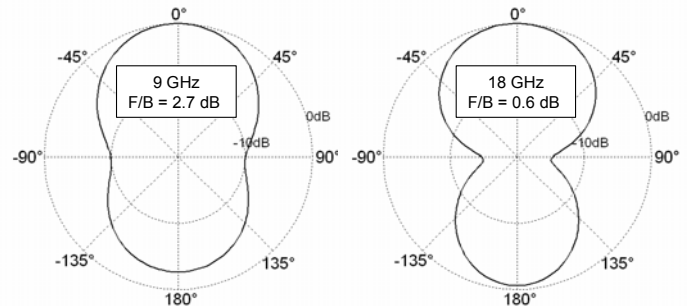

Fig. 21.   Radiation pattern of the conical spiral in the *xz* plane for two frequencies. Left-hand side: 9 GHz; Right-hand side: 18 GHz.

Considering that for most applications, the back side radiation is suppressed through a cavity, the design of a spiral can take advantage of a conformal design, even with the limited extent of the height (as opposed to classical conical spirals that have a sharp flare angle). However, for shapes that do not have an axial symmetry with respect to the center of the spiral, e.g. for surfaces with varying radii of curvatures in different directions, a degradation of the circular polarization can be expected.
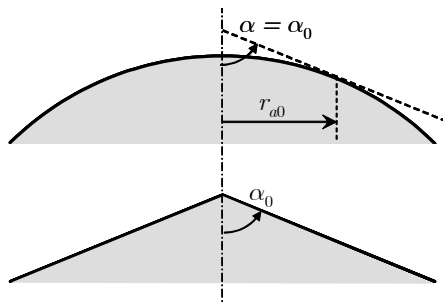
Fig. 22. Side views of the spherical and conical substrates. The flare angle α_o of the cone is defined in the bottom drawing. The tangential line to the sphere that forms the same angle α_o with the axis of the spiral occurs for an active radius r_a and is shown in the top drawing.

V. Conclusion

The FVTD method has been utilized for the simulation of various Archimedean spiral antennas with different substrate configurations. Although the presented radiating structures are challenging for most computational methods, the analysis with the FVTD method has been straightforward and did not impose any problems. The FVTD's unstructured mesh provides the geometrical flexibility to resolve the fine spiral structure on a thin substrate.

The FVTD method has also been used to investigate substrate effects on the radiation characteristics of an Archimedean spiral. Several variations in the substrate properties (permittivity, thickness) and shape (planar vs. non planar) have been studied. Conclusions have been drawn based on the simulated effective permittivity relevant for currents propagating along the spiral arms and considering the spiral active radiating region, i.e. where one spiral turn corresponds to one effective wavelength.

The effects caused by variations of the substrate permittivity and thickness of the planar configurations have been compared to CPS lines with comparable cross-sections (same gap width as inter-arm distance on the spiral). The comparison of the transverse field distribution on the spiral and on the CPS permits to understand the difference found in the effective permittivity for both geometries. Considering a CPS with broader conducting strips (i.e. same gap, but twice the strip width) gives a good approximation of the ε_{eff} on the spiral.

Three configurations of spirals on non-planar substrates with common geometrical shapes have been investigated. The effects on the antenna polarization and F/B ratio have demonstrated that the performance of non-planar configurations provide no substantial degradation of the radiation characteristics. In some configurations radiation characteristics are even improved.

As for the FVTD method it should be emphasized that the simulation of conformal structures represents the same computational load as that of a corresponding planar geometry. Simulations of configurations with multiple radii of curvatures in different directions require no algorithm modifications and are solely reduced to the problem of mesh generation.

References

[1] J.J. van Tonder, J.H. Cloete, "A study of an Archimedes spiral antenna", *IEEE Antennas and Propagat. Society Int. Symp. Dig.*, AP-S vol. 2, pp. 1302 – 1305, June 1994.

[2] H. Nakano, K. Nogami, S. Arai, H. Mimaki, J. Yamauchi, "A spiral antenna backed by a conducting plane reflector", *IEEE Trans. Antennas Propagat.*, vol. AP-34, pp. 1417-1423, June 1986.

[3] M.N. Afsar, Y. Wang, R. Cheung, "Analysis and measurement of a broadband spiral antenna", *IEEE Antennas Propagat. Mag.*, vol. 46, pp. 59-64, Feb. 2004.

[4] C.W. Penney, R.J. Luebbers, "Input impedance, radiation pattern, and radar cross section of spiral antennas using FDTD", *IEEE Trans. Antennas Propagat.,* vol. AP-42, pp. 1328 -1332, Sept. 1994.

[5] H. Nakano, M. Ikeda, K. Hitosugi, J. Yamauchi, "A spiral antenna sandwiched by dielectric layers", *IEEE Trans. Antennas Propagat.*, vol. AP-34, pp. 791-796, June 2004.

[6] D.S. Filipović, J.L Volakis, "Novel slot spiral antenna designs for dual-band/multiband operation", *IEEE Trans. Antennas Propagat.*, vol. AP-51, pp. 430-440, March 2003.

[7] N.K. Madsen, R.W. Ziolkowski, "A three-dimensional modified finite volume technique for Maxwell's equations", *Electromagnetics*, vol. 10, pp. 147-161, 1990.

[8] V. Shankar, A.H. Mohammadian, W.F. Hall, "A time-domain, finite-volume treatment for the Maxwell equations", *Electromagnetics*, vol. 10, pp. 127-145, 1990.

[9] P. Bonnet, X. Ferrieres, B.L. Michielsen, P. Klotz, J.L. Roumiguières, "Finite-Volume Time Domain Method", Chapter 9 in *Time domain electromagnetics*, edited by S.M. Rao, Academic Press, San Diego, 1999.

[10] C. Fumeaux, D. Baumann, P. Leuchtmann, R. Vahldieck, "A generalized local time-step scheme for efficient FVTD simulations in strongly inhomogeneous meshes", *IEEE Trans. Microwave Theory Tech.* MTT-52(3), pp. 1067-1076, 2004.

[11] D. Baumann, C. Fumeaux, P. Leuchtmann, R. Vahldieck, "Generalized-scattering-matrix extraction using the finite-volume time-domain (FVTD) method", *IEEE MTT-S Int. Microwave Symp. Dig.*, pp. 1701-1704, June 2004.

[12] B.C. Wadell, "Transmission Line Design Handbook", Artech House, Boston (1991).

Christophe Fumeaux received the diploma and Ph.D. degrees in physics from the Swiss Federal Institute of Technology (ETH) Zurich, Switzerland, in 1992 and 1997, respectively. His Ph.D. thesis on antenna-coupled infrared detectors was awarded the ETH Silver Medal of Excellence. From 1998 to 2000 he was post-doctoral researcher in infrared technology at the School of Optics (CREOL) of the University of Central Florida (UCF), Orlando. In 2000 he joined the Swiss Federal Office of Metrology in Bern, Switzerland, as a scientific staff member. Since 2001, he is a research associate at the Laboratory for Electromagnetic Fields and Microwave Electronics (IFH) at ETH Zurich. His current main research interest concerns computational electromagnetics in the time domain for numerical analysis of microwave circuits and antennas.

Dirk Baumann received the Dipl. Ing. degree in electrical engineering from the University of Karlsruhe, Germany, in 2001. Between Spring and Fall 2000 he did an internship at the Alaska SAR Facility (ASF) in Fairbanks, AK, working on the calibration of ASF's SAR processor. Currently he is working toward the Ph.D. degree in electrical engineering at the Laboratory for Electromagnetic Fields and Microwave Electronics (IFH), ETH Zurich, Switzerland. His research interests include numerical methods with emphasis on time domain techniques and their application to general electromagnetic problems.

Rüdiger Vahldieck received the Dipl. Ing. and the Dr. Ing. degrees in electrical engineering from the University of Bremen, Germany, in 1980 and 1983, respectively.
From 1984 to 1986 he was a Postdoctoral Fellow at the University of Ottawa, Canada. In 1986 he joined the Department of Electrical and Computer Engineering at the University of Victoria, British Columbia, Canada, where he became a Full Professor in 1991. During Fall and Spring of 1992-'93 he was a visiting scientist at the "Ferdinand-Braun-Institut für Höchstfrequenztechnik" in Berlin, Germany. In 1997 he accepted an appointment as Professor for electromagnetic field theory at the Swiss Federal Institute of Technology, Zurich, Switzerland, and became head of the Laboratory for Electromagnetic Fields and Microwave Electronics (IFH) in 2003. His research interests include computational electromagnetics in the general area of EMC and in particular for computer-aided design of microwave, millimeter wave and opto-electronic integrated circuits.
Professor Vahldieck is a Fellow of the IEEE. He received the J.K. Mitra Award of the IETE (in 1996) for the best research paper in 1995, and was co-recipient of the outstanding publication award of the Institution of Electronic and Radio Engineers in 1983. Since 1981 he has published more than 230 technical papers in books, journals and conferences, mainly in the field of microwave CAD. He is the Past-President of the IEEE 2000 International Zurich Seminar on Broadband Communications (IZS'2000) and since 2003 President and General Chairman of the international Zurich Symposium on Electromagnetic Compatibility. He is a member of the editorial board of the IEEE Transaction on Microwave Theory and Techniques. From 2000 until 2003 he served as an Associate Editor for the IEEE Microwave and Wireless Components Letters and is now the Editor-in-Chief effective Jan. 2004. Since 1992 he serves on the Technical Program Committee of the IEEE International Microwave Symposium, the MTT-S Technical Committee on Microwave Field Theory, and in 1999 on the TPC of the European Microwave Conference. From 1998 until 2003 Professor Vahldieck was the chapter chairman of the IEEE Swiss Joint Chapter on MTT, AP and EMC.